# Examining the structure and bonding in complex oxides using aberration-corrected imaging and spectroscopy

R. F. Klie, Q. Qiao, T. Paulauskas, Q. Ramasse, M. P. Oxley, and J. C. Idrobo

Phys. Rev. B **85**, 054106 — Published 10 February 2012

DOI: 10.1103/PhysRevB.85.054106

# Examining the structure and bonding in complex oxides using aberration-corrected imaging and spectroscopy

R.F. Klie, Q. Qiao, and T. Paulauskas
*University of Illinois at Chicago, Chicago, IL 60607*

Q. Ramasse
*SuperSTEM, Daresbury, UK*

M.P. Oxley and J.C. Idrobo
*Department of Physics and Astronomy, Vanderbilt University, Nashville, TN 37235, USA and*
*Materials Science and Technology Division, Oak Ridge National Laboratory, Oak Ridge, TN 37831, USA*

(Dated: January 27, 2012)

Our ability to directly characterize the atomic and electronic structures is crucial to developing a fundamental understanding of structure-property relationships in complex oxide materials. Here, we examine one specific example, the misfit-layered thermoelectric material, $Ca_3Co_4O_9$, which exhibits a high Seebeck coefficient governed by spin-entropy transport, as well as hopping mediated electron transport. However, the role of oxygen and its bonding with cobalt in the thermoelectric transport remains unclear. We use atomic-resolution annular bright field imaging (ABF) to directly image the oxygen sub-lattice, and combine our experimental data with multi-slice image calculations, to find that the oxygen atoms in the $CoO_2$ subsystem are highly ordered, while the Oxygen atomic columns are displaced in the $Ca_2CoO_3$ sub-system. Atomic-column resolved electron energy-loss spectroscopy (EELS) and spectrum image calculations are used to quantify the boding in the different sub-systems of the incommensurate $Ca_3Co_4O_9$. We find that the holes in the $CoO_2$ sub-system are delocalized, which could be responsible for the $p$-type conductivity found in the $CoO_2$ subsystem.

PACS numbers: 68.37.Ma, 79.20.Uv, 73.50.Lw, 71.20.Be
Keywords: STEM, annular bright field imaging, EELS, thermoelectric oxide

## I. INTRODUCTION

Thermoelectric materials, in particular thermoelectric oxides, have attracted increasing attention in recent years due to their exceptionally high Seebeck coefficients and high temperature stability.[1–8] In thermo-electric materials, a temperature gradient $\Delta T$ in an open circuit causes the diffusion of mobile charge carriers from the hotter to the cooler end of the sample. The charge accumulation then leads to the formation of a net electric field, which determines the Seebeck coefficient $S$. Fundamental to the field of thermo-electric materials is the need to optimize a variety of conflicting properties. The effectiveness of a thermoelectric material can be directly linked to the dimensionless figure of merit, given by $zT = (\frac{S^2\sigma T}{\kappa})$, which means that a large thermopower (absolute value of the Seebeck coefficient $S$), high electrical conductivity ($\sigma$), and low thermal conductivity ($\kappa$) are crucial for high-efficient thermo-electric materials.

$Ca_3Co_4O_9$, an incommensurately layered oxide, consists of two separate sub-systems, each fulfilling a different role in achieving high thermo-electric properties. Along the $c$-axis of $Ca_3Co_4O_9$, $CdI_2$-type $CoO_2$ layers are separated by a triple-layer of insulating rocksalt-type structure, where the $CoO_2$ acts as the highly conductive $p$-type electron crystal, while the insulating $Ca_2CoO_3$ acts as the phonon-glass and charge reservoir layers.[9]

The high Seebeck coefficient in $Ca_3Co_4O_9$[10] has been attributed to a number of different mechanisms, including large $m^*$ of the charge carriers due to the strong correlations in the $CoO_2$ sub-system, or the occurrence of a mixed-valence state in the $CoO_2$ layer.[11] While it has been recognized that understanding the interaction between the different sub-systems in $Ca_3Co_4O_9$ holds the key to understanding the exceptionally high thermoelectric properties of these incommensurately layered systems, there are only a few detailed structural or theoretical studies of $Ca_3Co_4O_9$ or related materials.[2,12–16] In particular, there is currently not a single detailed experimental study on the local structural disorder in the $Ca_2CoO_3$ layer, or the bonding between the $CoO_2$ and the $Ca_2CoO_3$ subsystems.

In this paper, we show a study of the local structure and bonding configuration of the $CoO_2$ and $Ca_2CoO_3$ subsystems using atomic-resolution Z-contrast, annular bright field (ABF) imaging, and electron energy-loss (EEL) spectrum imaging in aberration-corrected scanning transmission electron microscopy (STEM), combined with multi-slice image calculations and EEL spectrum image modeling. In particular, we will demonstrate that the position of the oxygen atomic columns in $Ca_3Co_4O_9$ can be directly visualized using the incoherent imaging technique ABF. Moreover, we will show how EELS spectrum imaging of the O $K$-edge can be used to plot the spatial distribution of the Co 3$d$, Ca 4$sp$ and Co 4$sp$ orbitals. Using these new methods, we find that it is now be possible to directly assess the effects

of doping and point defect on the local bonding and the interaction between the different $Ca_3Co_4O_9$ sub-systems as well as other complex oxide systems.

## II. METHODS

In this study, we have utilized both ABF, as well as high-angle annular dark field (HAADF) imaging techniques in the STEM to directly image the cation and anion sublattice in $Ca_3Co_4O_9$. It has been previously shown that atomic-resolution Z-contrast imaging can be used characterize the Ca and Co sublattice,[6,7], while the oxygen sublattice, which is believed to hold the key to the understanding of the high Seebeck coefficient in $Ca_3Co_4O_9$, has remained elusive. The oxygen sublattice has not been directly observed before because oxygen has a weak scattering intensity in the range of collection angles used for HAADF imaging.

However, the recently developed imaging mode known as ABF[17] (which is achieved by blocking the central unscattered electron beam and reducing the collection angle of the annular detector) now permits to detect and resolve weakly scattering elements in crystal lattice, including oxygen, nitrogen or even hydrogen,[17,18] without showing the typical contrast reversal as a function of defocus and sample thickness dependance artifact present in all conventional phase contrast images.[17]

The images and spectra shown in this paper were acquired using the aberration-corrected JEOL ARM200F, equipped with a 200 kV Schottky field emission gun, a high-angle annular dark field and an annular bright field detector, as well as a post-column Gatan Enfina EELS spectrometer. All images and spectra shown here were obtained with a 22 mrad probe convergence angle. The high-angle annular dark field (or Z-contrast images) were acquired using a 90 mrad inner detector angle, while the the annular bright-field (ABF) images were taken with a inner angle of 11 mrad and an outer detector angle of 22 mrad. The collection angle for the EELS spectra was 45 mrad.

The multi-slice image calculations were calculated using the QSTEM simulation suite.[19] For the $Ca_3Co_4O_9$ structures calculated in this paper, we have used the $(Ca_2CoO_3)_2(CoO_2)_3$ approximant (Figure 1(a) and 1(b)) with a total sample thickness of 14 nm. We have taken the effects of the electron probe size effects into account with a 0.07 Å FWHM Gaussian broadening of the final image and a 16 pixel interpolation from an original size of $40 \times 40$ in all calculations. Furthermore, we have used 30 frozen phonons using the atomic weight to approximate the displacements at room temperature of the high-angle annular dark field images. The convergence angle was set to 22 mrad for all calculations, while a collection angle of 11-22 mrad was used for the ABF images and a collection angle of 90-250 mrad for the HAADF images, in agreement with the experimental values. The aberrations coefficients for the 200kV JEOL ARM200 were approximated by using the values reported by Haider et al.[20]

The EELS spectrum images were calculated using a Bloch wave method[21,22] with absorption due to thermal diffuse scattering included.[23] The EELS scattering potential was evaluated using an isolated atomic model[24] Bound state wave functions are calculated using a Hatree-Fock code with relativistic corrections and bound continuum states are use a Hatree-Slater method.

## III. SAMPLE PREPARATION

The $Ca_3Co_4O_9$ samples in this study were synthesized using pulsed laser deposition (PLD). The ceramic targets were prepared from high-purity $CaCo_3$ and $Co_3O_4$ powders that were mixed stoichiometrically and the calcined at 880° C for 24 hours in flowing air.[12,25] Previous studies of these samples have shown that the $Ca_3Co_4O_9$ films are stoichiometric and free of any measurable impurities.[6,7] In addition, measurements of the Seebeck coefficient, $S$, as a function of temperature have found the typical behavior with a linear increase of $S$ up to $T = 170$ K followed by a nearly constant plateau at $S = 135$ $\mu$V/K between $T = 170$ K and $T = 430$ K.[26]

## IV. RESULTS AND DISCUSSION

Figure 2(a) shows an atomic-resolution Z-contrast image of $Ca_3Co_4O_9$ in the [100] direction. In this orientation, the different sub-systems of the $CoO_2$ and the rocksalt $Ca_2CoO_3$ layers can be directly distinguished. The $CoO_2$ layers appear as the brighter atomic columns on the top and bottom of Figure 2(a), while the triple-rocksalt layer is sandwiched between two $CoO_2$ layers. Due to the higher density of Co atoms along the (100) direction, the Co columns appear brighter in the $CoO_2$ layer than in the $Ca_2CoO_3$ layers. In addition, the Co atomic columns in the center of the $Ca_2CoO_3$-layer appear blurred, which has been previously attributed to a structural modulation of the Co atomic-positions along the $b$ direction.[6,27] This modulation will also contribute to a lower than expected Co-column intensity as a result of increasing dechanneling of the incoming electron probe.

Figure 2(b) shows an ABF image taken simultaneously with the Z-contrast image in Figure 2(a). All the atomic columns shown in the Z-contrast image can also be seen in the ABF image. The most prominent difference between the two micrographs is that the image contrast in the ABF image is inverted compared to the Z-contrast image. To simplify this discussion, Figure 2(c) shows the ABF image with inverted image contrast. This image clearly shows additional intensities compared to the Z-contrast image, specifically, it appears that the O atomic columns in the $CoO_2$ are resolved in the ABF, as well as some additional intensity between the Co atoms in the $Ca_2CoO_3$-layer. The simulated HAADF and ABF images for $Ca_3Co_4O_9$ on the [100] orientation are shown in Figure 3(a) and 3(b). Overall, both the simulated HAADF and the ABF images agree well with the experimental images shown in Figure 2(a) and 2(b). The imaging calculations clearly demonstrate that the oxygen atomic columns should not be visible in the HAADF images, but show up as clear signals above and below the Co-atomic columns of the $CoO_2$ layers in the calculated ABF image. Such intensities are also visible in Figure 2(b), which shows that the oxygen atoms in the $CoO_2$ sub-systems are not disordered, as suggested by earlier studies.[28] However, the intensity of the Co atomic columns in the $Ca_2CoO_3$ sub-systems appears significantly brighter in the simulation compared to the experiments. Moreover, the experimental HAADF and ABF images (Figure 2(a) and 2(c)) show additional, diffuse signal between the Co atomic columns, which is not seen in the calculations. This difference indicates a modulation of the Co atomic-positions along the $b$ direction, as reported earlier.[6,15,27]

An intensity line profile across a unit-cell of $Ca_3Co_4O_9$ along the $c$-axis is shown in Figure 4, comparing the image intensity for the different atomic columns in the Z-contrast and in the inverted ABF image. It can be clearly seen, that the image intensity of the $CoO_2$ column in the Z-contrast image is significantly higher than the Co or Ca columns, since the image intensity in Z-contrast imaging is directly proportional to $Z^n$ ($n \sim 1.8$). It is interesting to note here that the intensity in the inverted ABF image for the $CoO_2$ and for the Co columns are very similar, and only the Ca atomic columns have a slightly lower intensity. In addition, the O atomic columns can be seen in the line profile as the two distinct shoulder adjacent to the Co peak.

It was previously shown that the ABF image does not exhibit any features of a coherent image[17] and the ABF images shown here exhibit no contrast reversal as a function of sample thickness or spatial frequency. However, due to the different intensity forming mechanism of ABF imaging compared to HAADF imaging, a direct quantitative analysis of the atomic columns does not appear to be possible. In particular, both the $CoO_2$ and the Co atomic columns exhibit the same intensity in the ABF images, but the difference in average atomic mass is clearly visible in the Z-contrast images (Figure 4).

Figure 5(a) shows an atomic-resolution Z-contrast image of $Ca_3Co_4O_9$ [110]. In this orientation, the $CoO_2$ atomic columns cannot be resolved since the interatomic distances in the Co and the O layers (Figure 1(b)) are too small to be distinguished, even with the aberration-corrected electron probe. Therefore, both the Co and O layers appear as a continuous lines. On the other hand, the individual atomic columns in the rocksalt $Ca_2CoO_3$-layers can be clearly seen in both the Z-contrast image and the simultaneous ABF image (Figure 5(b)). The inverted ABF image (Figure 5(c)) again shows additional image intensities that were not visible in the Z-contrast images. The O atomic columns in the Ca layers of the rocksalt $Ca_2CoO_3$ can be directly identified, and it can be seen that the position of the O atoms in slightly displaced towards the CoO-layers with respect to the Ca. The location of the atomic layer in the $CoO_2$-subsystem can also be seen in the ABF images as the broader lines adjacent to the line which represents the Co atomic layers.

Multi-slice image simulations are again performed using the structure shown in Figure 1(b). It can be seen than both the HAADF (Figure 6(a)) as well as the ABF image (Figure 6(b)) match the experimental images shown in Figure 5. It is interesting to note here that while the O atomic column in the CaO layers can be clearly seen in the images, the O atoms between the Co atomic columns in the CoO layers are not distinguishable. This can be again attributed to the modulations in the CoO layers, previously reported.[6,15,27]

Atomic-resolution EELS spectra of the O $K$-edge from the Ca, Co, O sites, as well as from the $CoO_2$ layers in $Ca_3Co_4O_9$ [110] are shown in Figure 7. Each spectrum represents the sum of 4-8 individual spectra taken with an acquisition time of 0.1 s and a dispersion of 0.5 eV/pixel. Although the spectra have a low signal to noise ratio due to the short exposure time, a pre-peak feature (located at 530 eV) of the O $K$-edge can be clearly distinguished. As previously reported, the O $K$-edge pre-peak intensity is highest in the $CoO_2$ columns and lowest on the Ca atomic columns.[6] Using the integrated intensities of the O $K$-edge, the Co $L$-edge, and the Ca $L$-edge, we can now plot the distribution of the different elemental concentration as a function of position within the $Ca_3Co_4O_9$ unit-cell. The resulting spectrum image is shown as an insert in Figure 5(a), and a comparison with the ABF image (Figure 5(c)) clearly indicates that the O atomic-columns in the $Ca_2CoO_3$-layers are displaced towards the Co. Moreover, we also can see that the Co columns in the center of the $Ca_2CoO_3$-layers appear elongated along the $ab$-plane. Yet, such a distortion was not directly observed in either the HAADF nor the ABF image. The result indicates the slight disorder on the Co and O sublattice within the CoO layers.

Next, we characterize the bonding within the $Ca_3Co_4O_9$ unit-cell. It was previously demonstrated that the O $K$-edge of $Ca_3Co_4O_9$ can be separated into three distinct regions, starting with the pre-peak which spans from 530 -

536 eV, followed by a first main peak located between 536 - 542 eV, and a second broad peak between 542 eV and 549 eV. The O $K$-edge pre-peak (labeled peak $A$ in Figure 7) stems from electron transitions from the O 1$s$ into the hybridized O 2$p$-Co 3$d$ orbitals.[6] The additional splitting of the O $K$-edge pre-peak, associated with transitions into the $a_{1g}$ and the $e_g$ orbitals, cannot be distinguished in the spectra shown in Figure 7 since the dispersion and exposure time was optimized for spectrum imaging rather than energy resolution. Recent studies using an cold-field emission electron source in an aberration-corrected TEM instrument have demonstrated that the increased energy resolution of the cold-field emission gun is sufficient to resolve the splitting of the O $K$-edge pre-peak into the $a_{1g}$ and the $e_g$ orbitals.[26] The main peak is labeled $B$ (535 - 542 eV) and has been associated with transition into the O 2$p$-Ca 3$d$ hybridized orbitals,[2] the second broad feature of the O $K$-edge (labeled peak $C$) has been attributed to transitions into the O 2$p$-Co 4$sp$ orbitals.[6]

To further study the spatial distribution of the O $K$-edge near-edge fine-structure within the $Ca_3Co_4O_9$ unit cell, we acquired a 480 × 480 pixel EELS spectrum image with a dwell time of 0.1 $\mu$s per pixel. Figure 8 shows the resulting spectrum image, where the relative integrated intensities of the pre-peak (peak $A$, Figure 8(a)), peak $B$ (Figure 8(b)) and $C$ (Figure 8(c)) are plotted as a function of position. All the integrated peak-intensities are normalized to the total intensity of the O $K$-edge intensity (integrated from 525 - 560 eV) to avoid any contribution from the relative oxygen concentration gradient.

It is interesting to note here that the different peaks in the O $K$-edge exhibit different spatial distributions across the $Ca_3Co_4O_9$ unit cell. More specifically, the pre-peak (Figure 8(a) appears to be strongest in the $CoO_2$ sub-system, as well as on the oxygen atomic columns in the CaO layers. On the other hand, peak $B$ appears to be localized on the Ca atomic columns, while the peak labeled $C$ is showing the highest intensities on the Co columns of the $Ca_2CoO_3$ sub-system, as well as on the oxygen columns of the CaO layer and less localized intensity in the entire $CoO_2$ sub-system. Figure 9(a) and 9(b) show the calculated spectrum image intensity distribution for the O $K$-edge integrated over a large range of energy (530-560 eV) as a function of sample thickness. In agreement with earlier papers,[29–31] these calculations clearly demonstrate that the O $K$-edge signal should be strongly localized on the oxygen atomic columns in the $Ca_2CoO_3$ sub-systems, as well as in the oxygen layers of $CoO_2$ similar to what is observed in Figure 5(a). For none of the sample thicknesses presented in this paper we expect a delocalization of the integrated O $K$-edge signal to the extend seen for the individual peaks in the O $K$-edge fine-structure (shown in Figures 8(a) - 8(c)).

To better understand the different spatial distributions of the O $K$-edge near-edge fine-structure peaks, we need to examine the final-state orbitals that contribute to the peaks $A$, $B$, and $C$. Since the O $K$-edge pre-peak intensity scales with both the concentration of mobile holes as well as the Co valence in $Ca_3Co_4O_9$[6], one could expect the O $K$-edge pre-peak intensity to be highest in the $CoO_2$ sub-system, as shown in Figure 8(a). The high intensity of the O $K$-edge pre-peak intensity on the oxygen atomic columns of the CaO layers can be explained by the bonding of those oxygen atoms with the Co atoms in the center of the $Ca_2CoO_3$ system. It is interesting to notice, however, that the oxygen atomic columns in the center of the $Ca_2CoO_3$ layers do not show any localized increase in the pre-peak intensity, which could be an effect of the local disorder on the oxygen sub-lattice in this layer. The pre-peak intensity is lowest on the Ca and the Co atomic columns in the $Ca_2CoO_3$-layer, indicating that the hybridized O 2$p$-Co 3$d$ orbitals are clearly localized on the oxygen atomic-columns.

Peak $B$, and therefore the hybridized O 2$p$-Ca 3$d$ orbitals appear to be localized on the Ca atoms, while exhibiting the lowest intensity on the O and Co atomic columns. Moreover, the spatial distribution of these hybridized orbitals appears to be spherical around the Ca atoms. The third peak of the O $K$-edge, peak $C$, which is attributed to transitions into the O 2$p$ - Co 4$sp$ orbitals shows a non-spherical symmetry in the $Ca_3Co_4O_9$ unit-cell. In fact, and the peak intensity distribution resembles the symmetry of the $sp$-orbital shape with significant intensity on the Co atoms and between the O and the Co atoms. Due to the large convergence angle of the incoming electron probe, only in orbitals with symmetry perpendicular to the incoming electron beam direction are measured.[32,33] It is further interesting to note that the intensity of peak $C$ in the $CoO_2$ sub-system exhibits a different distribution compared to that of peak $A$. More specifically, it seems that while the pre-peak intensity is delocalized within the $CoO_2$ layers, the intensity of peak $C$ appears to increase towards the central Co atomic layer, consistent with the behavior found in the $Ca_2CoO_3$ sub-system. While it is not possible to resolve the Co or O atomic columns in the $CoO_2$ sub-system in this orientation of $Ca_3Co_4O_9$, one can still conclude that the O $K$-edge pre-peak, or more specifically, the associated electron hole concentration appears delocalized across the entire thickness of the $CoO_2$ layer. This delocalization of holes can explain the high $p$-type conductivity found in the $CoO_2$ layers, which is partially responsible for the high Seebeck coefficient, $S$, of $Ca_3Co_4O_9$.

Finally, the apparent bonding between the $Ca_2CoO_3$ and the $CoO_2$ appears to be very small, since none of the O $K$-edge fine-structure peaks plotted in Figure 8 bridge from either sub-system to the other. In fact, earlier studies of $Ca_3Co_4O_9$ thin films have shown that the interlayer bonding in $Ca_3Co_4O_9$ is very weak, and interfacial strain competes with the van-der-Waals bonding between the $Ca_2CoO_3$ and $CoO_2$ layers resulting in an altered stacking sequences in close proximity to the substrate-film interface.[34]

## V. CONCLUSIONS

In summary, we have demonstrated that by using atomic-resolution ABF and HAADF imaging in combination with EEL spectrum imaging in an aberration-corrected STEM all the constituent atoms, including light elements such as oxygen, can be directly imaged in complex-oxide systems, such as the incommensurately-layered $Ca_3Co_4O_9$. In addition, we have shown that the spatial distribution of different orbitals can be directly visualized using measured differences in the localization of the O $K$-edge near-edge fine-structure peaks. By combining our experimental data with multi-slice image calculations, as well as EELS spectrum image modeling of the intensity localization, we conclude that the oxygen atomic columns in the $CoO_2$ subsystem of $Ca_3Co_4O_9$ do not exhibit any disorder, in contrast to earlier reports. However, we find that the O $K$-edge pre-peak, which is a direct measure of the mobile-hole concentration, is not localized on either the O or the Co layers in $CoO_2$ indicating the delocalized nature of the holes in this layer, exhibiting $p$-type electrical conductivity. Moreover, we find that the oxygen atomic columns in the CaO of the $Ca_2CoO_3$ subsystem are displaced towards the Co atomic columns, and that these O atomic-columns exhibit strong $sp$-type bonding with the central Co atoms. In addition, we find that the oxygen atomic-columns in the CoO layer are disordered. All these feature can be used to explain the suppression of in-plane phonon-modes, which are believed to be responsible for the relatively low thermal conductivity, found in $Ca_3Co_4O_9$.

Future research will focus on combining the kind of experimental data presented here with first-principles calculations to further explore the bonding in this complex, incommensurately layered systems. Using the combination of ABF imaging and EELS spectrum imaging with modeling, the effects of dopants or defects can now be directly shown on the the spatial distribution of different charge densities, as well as on the anion and cation sublattices. More specifically, in $Ca_3Co_4O_9$ the concentration of mobile holes and their location in the $Ca_3Co_4O_9$ unit cell will have a crucial influence on the thermoelectric properties of the material, and to our understanding of how these highly complex oxide systems, with surprisingly high thermo-power, function.

### Acknowledgements

The authors would like to thanks T. Isabell from JEOL Company for their help in acquiring the data. This work was supported by the National Science Foundation under grants number DMR-0846748 (RFK, QQ, TP) and DMR-0938330 (MPO), and by ORNL's Shared Research Equipment (SHaRE) User Facility, which is sponsored by the DOE Office of Basic Energy Sciences (JCI).

[1] W. Koshibae, K. Tsutsui, and S. Maekawa, Physical Review B **62**, 6869 (2000).
[2] R. Asahi, J. Sugiyama, and T. Tani, Phys. Rev. B **66**, 155103 (2002).
[3] T. Takeuchi, T. Kondo, K. Soda, U. Mizutani, R. Funahashi, M. Shikano, S. Tsuda, T. Yokoya, S. Shin, and T. Muro, Journal of Electron Spectroscopy and Related Phenomena **137**, 595 (2004).
[4] W. S. Seo, S. Lee, Y. Lee, M. H. Lee, Y. Masuda, and K. Koumoto, Journal Of Electron Microscopy **53**, 397 (2004).
[5] T. Takeuchi, T. Kondo, T. Takami, H. Takahashi, H. Ikuta, U. Mizutani, K. Soda, R. Funahashi, M. Shikano, M. Mikami, et al., Physical Review B **69**, 125410 (2004).
[6] G. Yang, Q. Ramasse, and R. F. Klie, Physical Review B **78**, 153109 (2008).
[7] G. Yang, Q. Ramasse, and R. F. Klie, Applied Physics Letters **94**, 093112 (2009).
[8] G. D. Tang, Z. H. Wang, X. N. Xu, L. Qiu, L. Xing, and Y. W. Du, Journal of Materials Science **45**, 3969 (2010).
[9] M. S. Dresselhaus, G. Chen, M. Y. Tang, R. G. Yang, H. Lee, D. Z. Wang, Z. F. Ren, J. P. Fleurial, and P. Gogna, Advanced Materials **19**, 1043 (2007).
[10] Y. Miyazaki, K. Kudo, M. Akoshima, Y. Ono, Y. Koike, and T. Kajitani, Japanese Journal Of Applied Physics Part 2-Letters **39**, L531 (2000).
[11] I. Terasaki, Y. Sasago, and K. Uchinokura, Physical Review B **56**, 12685 (1997).
[12] Y. F. Hu, W. D. Si, E. Sutter, and Q. Li, Applied Physics Letters **86** (2005).
[13] W. Koshibae and S. Maekawa, Physical Review Letters **87**, 236603 (2001).
[14] Y. Wakisaka, S. Hirata, T. Mizokawa, Y. Suzuki, Y. Miyazaki, and T. Kajitani, Physical Review B **78**, 235107 (2008).
[15] T. A. Tyson, Z. Chen, Q. Jie, Q. Li, and J. J. Tu, Physical Review B **79**, 024109 (2009).
[16] A. Rebola, R. F. Klie, and S. Ö˘ güt (2011).
[17] S. Findlay, N. Shibata, H. Sawada, E. Okunishi, Y. Kondo, and Y. Ikuhara, Ultramicroscopy **110**, 903 (2010).
[18] R. Ishikawa, E. Okunishi, H. Sawada, Y. Kondo, F. Hosokawa, and E. Abe, Nat Mater **10.1038/nmat2957** (2011).
[19] C. Koch, Ph.D. thesis, Arizona State University (2002).
[20] M. Haider, S. Uhlemann, and J. Zach, Ultramicroscopy **81**, 163 (2000).
[21] L. J. Allen, S. D. Findlay, A. R. Lupini, M. P. Oxley, and S. J. Pennycook, Physical Review Letters **91**, 105503 (2003).

[22] L. J. Allen and T. W. Josefsson, Phys. Rev. B **52**, 3184 (1995).
[23] L. J. Allen and C. J. Rossouw, Phys. Rev. B **39**, 8313 (1989).
[24] M. P. Oxley and L. J. Allen, Phys. Rev. B **57**, 3273 (1998).
[25] Y. F. Hu, E. Sutter, W. D. Si, and Q. Li, Applied Physics Letters **87** (2005).
[26] R. F. Klie, Q. Qiao, T. Paulauskas, A. Gulec, A. Rebola, S. Ögüt, M. Prange, J. Idrobo, S. Pantelides, S. Kolesnik, et al., Unpublished (2011).
[27] H. Muguerra, D. Grebille, and F. Bouree, Acta Crystallographica Section B-Structural Science **64**, 144 (2008).
[28] Y. Miyazaki, M. Onoda, T. Oku, M. Kikuchi, Y. Ishii, Y. Ono, Y. Morii, and T. Kajitani, Journal of the Physical Society of Japan **71**, 491 (2002).
[29] E. Cosgriff, M. Oxley, L. Allen, and S. Pennycook, Ultramicroscopy **102**, 317 (2005).
[30] M. Varela, M. P. Oxley, W. Luo, J. Tao, M. Watanabe, A. R. Lupini, S. T. Pantelides, and S. J. Pennycook, Physical Review B **79** (2009).
[31] M. P. Oxley and S. J. Pennycook, Micron **39**, 676 (2008).
[32] J. Yuan, R. S. Liu, P. P. Edwards, N. Browning, and L. M. Brown, Physica C **185**, 1059 (1991).
[33] R. F. Klie, Y. Zhu, G. Schneider, and J. Tafto, Appl. Phys. Lett. **82**, 4316 (2003).
[34] Q. Qiao, A. Gulec, T. Paulauskas, S. Kolesnik, B. Dabrowski, M. Ozdemir, C. Boyraz, D. Mazumdar, A. Gupta, and R. F. Klie, Journal of Physics: Condensed Matter **23**, 305005 (2011).

(a)(b)

FIG. 1: (Color online) Atomic structure of the $(Ca_2CoO_3)_2(CoO_2)_3$ approximant used for image and EELS calculations (a) in the [100] and (b) in the [110] orientation.

(a)(b)(c)

FIG. 2: (a) and( b) show simultaneous Z-contrast and annular bright field images, respectively, of $Ca_3Co_4O_9$ [100]. (c) ABF image with inverted contrast. Both Z-contrast and ABF images show the incommensurate structure of $Ca_3Co_4O_9$ along the $c$ axis.

(a)(b)

FIG. 3: Simulated (a) high-angle annular dark field and (b) annular bright field images of $Ca_3Co_4O_9$ [100].

FIG. 4: (Color online) Intensity line profile from the HAADF and the inverted ABF image across one unit-cell of $Ca_3Co_4O_9$. The different apparent intensities of the $CoO_2$ columns is an artifact of the incommensurate structure of $Ca_3Co_4O_9$ and the straight line of the intensity profile.

(a)(b)(c)

FIG. 5: (Color online) (a) Z-contrast image of $Ca_3Co_4O_9$ [110] and (b) simultaneous annular bright field image; (c) ABF image with inverted contrast. The bright field image clearly shows the location of the oxygen atomic columns, and the asymmetry of these atomic planes in the $Ca_2CoO_3$-layers. Insert in (a): EELS spectrum image showing the integrated O $K$-edge (red), Co $L$-edge (blue) and Ca $L$-edge (green).

(a)(b)

FIG. 6: Simulated (a) high-angle annular dark field and (b) annular bright field images of $Ca_3Co_4O_9$ [110].

FIG. 7: (Color online) Atomic-columns resolved EELS from different positions inside the $Ca_3Co_4O_9$ unit-cell.

(a)(b)(c)

FIG. 8: Spectrum images showing the spatial distribution of the (a) O $K$-edge pre-peak $A$ (b) peak $B$ and (c) peak $C$ intensities. All the integrated intensities are normalized to the integrated intensity of the first 30 eV of the O $K$-edge.

(a)(b)

FIG. 9: Calculated spectrum image intensity distribution for the integrated O $K$-edge of $Ca_3Co_4O_9$ [110] using a sample thickness of (a) 10 nm and (b) 30 nm

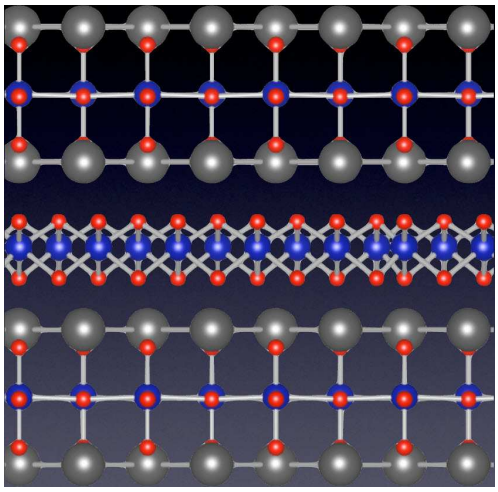

(a)

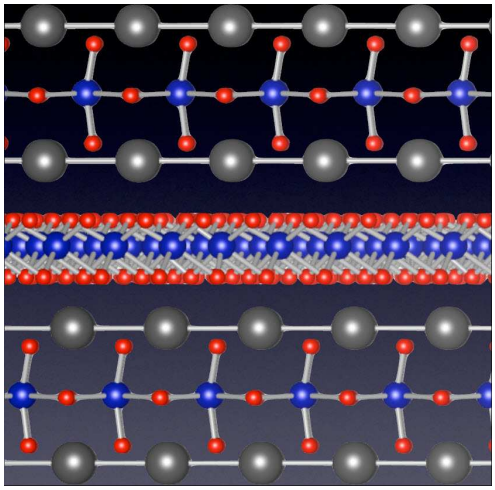

(b)

Figure 1 LR12677B 27Jan2012

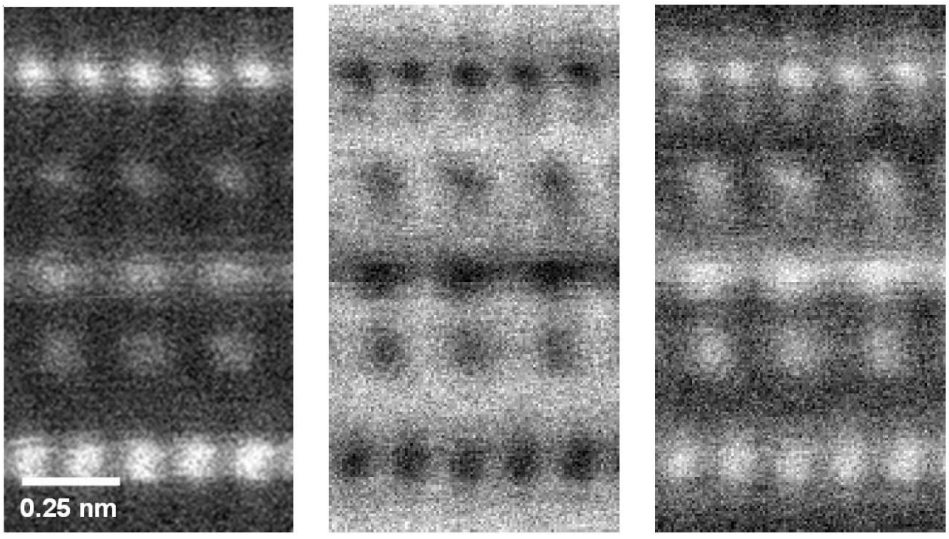


(a) (b) (c)

Figure 2 LR12677B 27Jan2012

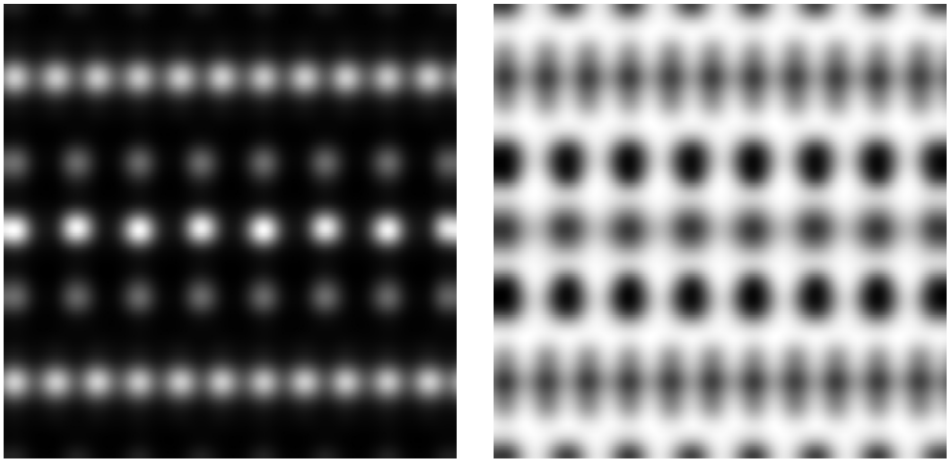

(a) (b)

Figure 3 LR12677B 27Jan2012

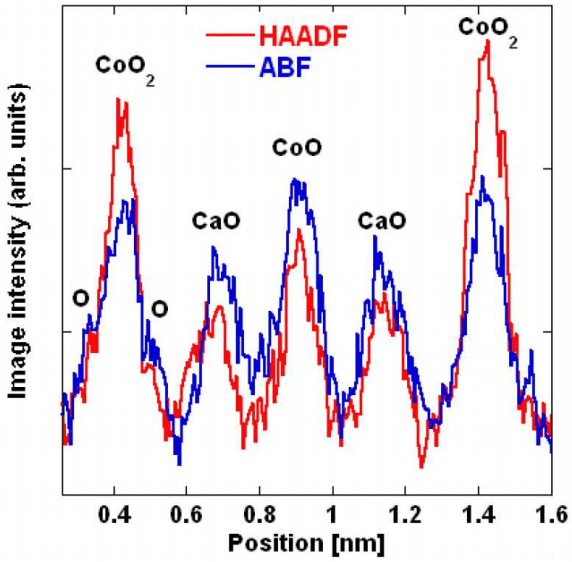


Figure 4 LR12677B 27Jan2012

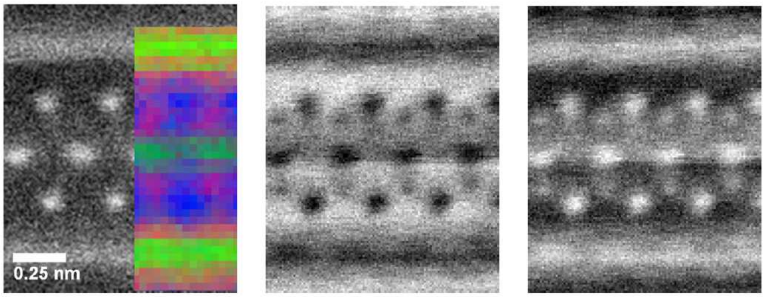


(a) (b) (c)

Figure 5 LR12677B 27Jan2012

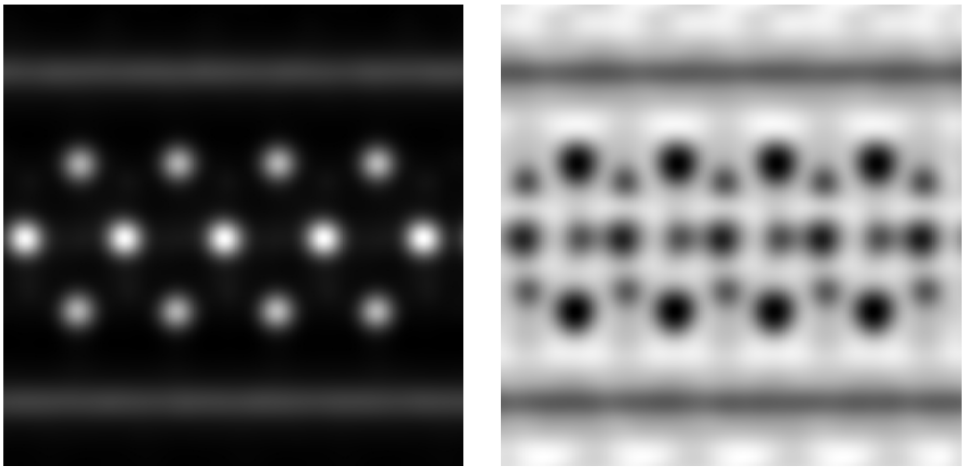

(a) (b)

Figure 6 LR12677B 27Jan2012

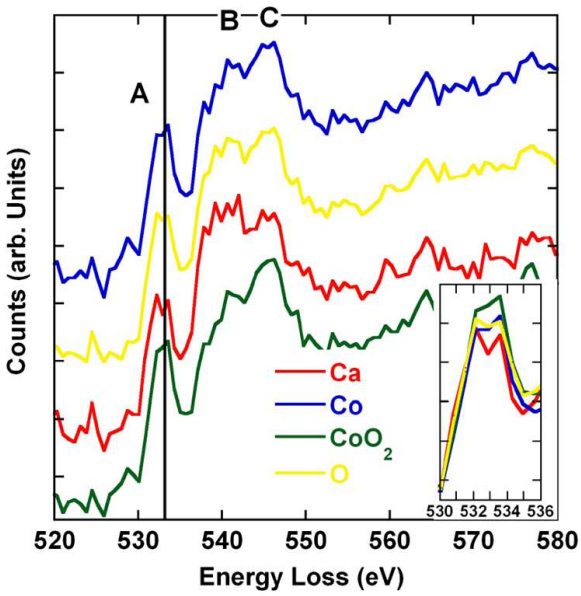


Figure 7 LR12677B 27Jan2012

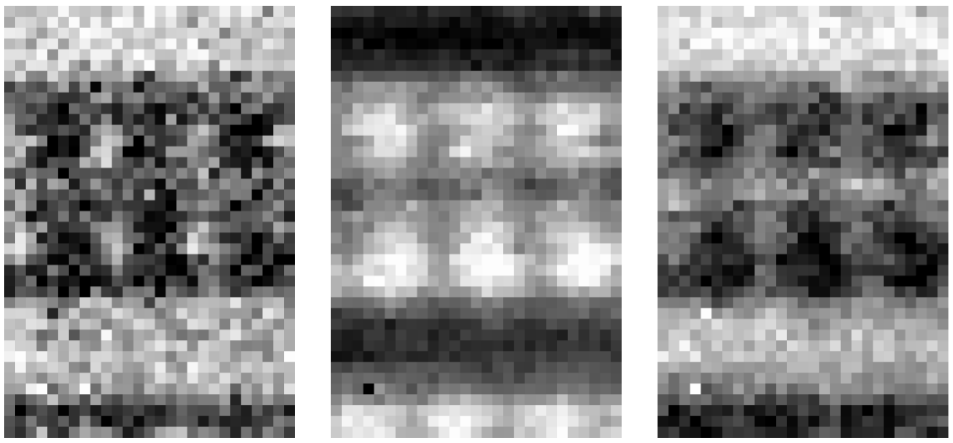

(a) (b) (c)

Figure 8 LR12677B 27Jan2012

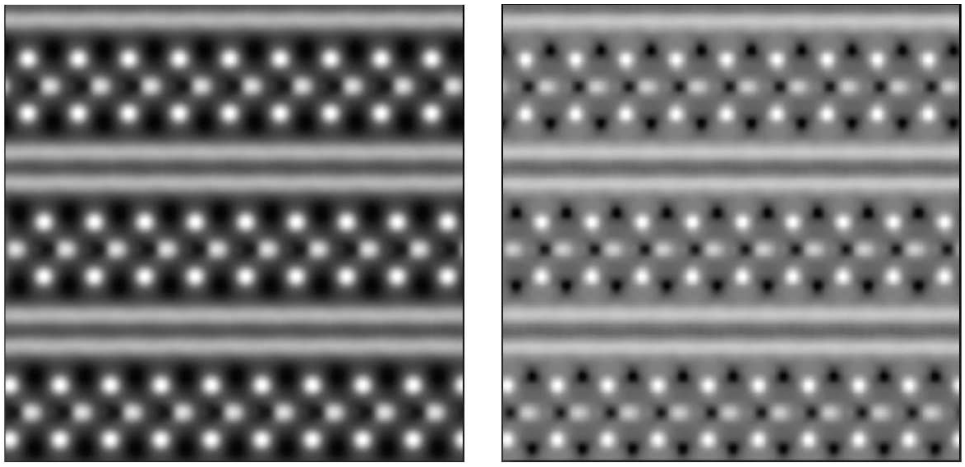

(a) (b)

Figure 9 LR12677B 27Jan2012